

# Declining dry deposition of NO<sub>2</sub> and SO<sub>2</sub> with diverse spatiotemporal patterns in China from 2013 to 2018

Kaiyue Zhou<sup>a</sup>, Yu Zhao<sup>a,b,\*</sup>, Lin Zhang<sup>c</sup>, Mengxiao Xi<sup>a,d</sup>

<sup>a</sup> State Key Laboratory of Pollution Control & Resource Reuse and School of the Environment, Nanjing University, Nanjing, Jiangsu, 210023, China

<sup>b</sup> Jiangsu Collaborative Innovation Center of Atmospheric Environment and Equipment Technology (CICAET), Nanjing University of Information Science & Technology, Nanjing, Jiangsu, 210044, China

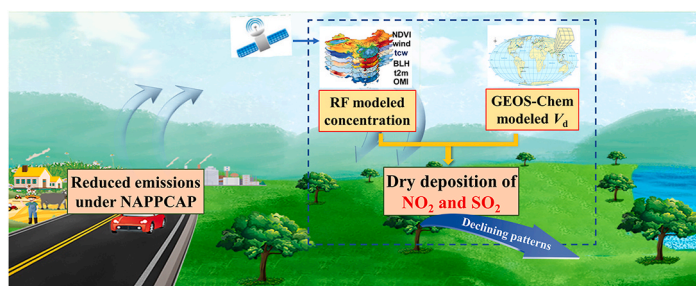
<sup>c</sup> Laboratory for Climate and Ocean-Atmosphere Sciences, Department of Atmospheric and Oceanic Sciences, School of Physics, Peking University, Beijing, 100871, China

<sup>d</sup> Environmental Big Data Science Center, Research Institute for Environmental Innovation Suzhou Tsinghua, Suzhou, Jiangsu, 215163, China

## HIGHLIGHTS

- China's Dry deposition was estimated based on the RF-derived concentration and CTM-simulated  $V_d$ .
- The NO<sub>2</sub> dry deposition was found larger in east China while SO<sub>2</sub> in north.
- NO<sub>2</sub> dry deposition declined slower in developed regions from 2013 to 2018, while SO<sub>2</sub> declined faster.
- Bigger reduction in SO<sub>2</sub> dry deposition was found than NO<sub>2</sub> due to controls on coal burning emissions.
- Growth in transportation and industrial capacity weakened the benefit of emission control on NO<sub>2</sub>.

## GRAPHICAL ABSTRACT



## ARTICLE INFO

### Keywords:

Dry deposition  
Random forest  
Air pollution control  
Spatiotemporal pattern

## ABSTRACT

The nitrogen and sulfur deposition results in damages on ecosystems, while the lack of direct observation on dry deposition limits our understanding of the total deposition. This study aimed to improve the methodology and estimates of NO<sub>2</sub> and SO<sub>2</sub> dry deposition in China and to explore the efficacy of China's recent emission control measures on dry deposition at the national and regional scales. We combined the random forest algorithm and the GEOS-Chem chemical transport model to predict the dry deposition fluxes of NO<sub>2</sub> and SO<sub>2</sub> and their inter-annual variabilities during 2013–2018 in mainland China. The annual NO<sub>2</sub> dry deposition ranged between 2.1 and 3.1 kg N ha<sup>-1</sup> yr<sup>-1</sup>, with an annual reduction rate of 0.21 kg N ha<sup>-1</sup> yr<sup>-1</sup> over this period. The areas with large deposition were located in the east, while the biggest reduction existed in the relatively clean Tibet Plateau region. The annual SO<sub>2</sub> dry deposition ranged between 7.5 and 18.4 kg S ha<sup>-1</sup> yr<sup>-1</sup>, with the annual reduction rate at 2.4 kg S ha<sup>-1</sup> yr<sup>-1</sup>. Both the magnitude and relative reduction in the north were generally larger than the south. Regarding the four typical economically developed regions, the NO<sub>2</sub> deposition declined slower than the national average, while SO<sub>2</sub> generally declined faster than or equivalently to the national average, except for Pearl River Delta. The reduced emissions attributed to the national action on air pollution control were identified as an important reason for the declining deposition. However, the increased traffic and industrial capacity in the east weakened its benefit on NO<sub>2</sub>.

\* Corresponding author. State Key Laboratory of Pollution Control & Resource Reuse and School of the Environment, Nanjing University, Nanjing, Jiangsu, 210023, China.

E-mail address: [yuzhao@nju.edu.cn](mailto:yuzhao@nju.edu.cn) (Y. Zhao).

<https://doi.org/10.1016/j.atmosenv.2021.118655>

Received 19 April 2021; Received in revised form 29 July 2021; Accepted 2 August 2021

Available online 5 August 2021

1352-2310/© 2021 Elsevier Ltd. All rights reserved.

## 1. Introduction

China's swift growth in economy and energy consumption have resulted in high emissions of nitrogen oxides (NO<sub>x</sub>) and sulfur dioxide (SO<sub>2</sub>), and thereby substantial deposition of nitrogen and sulfur. China was identified as one of the regions with the most serious atmospheric deposition (Liu et al., 2017; Zhang et al., 2021a), and consequent harmful impacts have been found for ecosystems and human, including soil and water acidification (Ti et al., 2018; Zhu et al., 2016), vegetation damage (Zhu et al., 2020b), reduced biodiversity (Deng et al., 2018) and increased greenhouse gas emissions (Lu et al., 2021; Zhu et al., 2020a).

Atmospheric deposition includes the dry and wet scavenging processes. Dry deposition is a process caused by turbulent diffusion, gravity deposition and molecular diffusion in the atmosphere without precipitation, while wet deposition is by means of rain or snow (González Benítez et al., 2009; Liu et al., 2020). In China, wet deposition that has been intensively studied attributed to relatively easy observation and sufficient monitoring sites (Jia et al., 2014; Liu et al., 2013; Yu et al., 2019). For example, Liu et al. (2013) found a significant growth in bulk nitrogen deposition across China between 1980 and 2010 based on historical observation data. Dry deposition was estimated to account for 20%–70% of the total deposition in many areas of China (Kuang et al., 2016; Xu et al., 2015; Zhang et al., 2012), and ignoring it could result in massive underestimation in the total deposition flux (Shen et al., 2013; Wu et al., 2018). Particularly NO<sub>2</sub> was found to account for averagely 25% of nitrogen dry deposition, and the provincial-level value could reach 43% in the east of the country (Vet et al., 2014; Xu et al., 2015, 2018a). SO<sub>2</sub> was the most important species in sulfur dry deposition, with its mass fraction ranging 72–98% (Luo et al., 2016). Influenced by the changing human activity, atmospheric conditions and underlying surfaces, dry deposition could be unevenly distributed in space and vary between years. To better understand the risks of atmospheric deposition across the country, therefore, it is a great necessity to capture the spatiotemporal patterns and the main control factors of dry deposition of NO<sub>2</sub> and SO<sub>2</sub>.

There was currently little direct observation on dry deposition in China because it was easily affected by multiple meteorological and environmental factors, such as temperature, relative humidity, surface roughness and turbulent boundary layer transport process (Pan et al., 2012; Tarnay et al., 2001; Xu et al., 2018b). Micrometeorological methods can be used for direct observation, including eddy covariance (Geddes and Murphy, 2014), aerodynamic gradient method (Ke et al., 2020), and relaxed eddy accumulation (Wei et al., 2020). Due to the need of extremely fast response instrument and uniform underlying surface, those methods are difficult to be intensively applied for long terms or in broad regions. Instead, indirect ways, including chemical transport modeling (CTM) and the inferential method, have been used in quantifying dry deposition at national or regional scale, e.g., EMEP (European Monitoring and Evaluation Programme in Europe; Simpson et al., 2012) CASTNET (Clean Air Status and Trends Network/the National Atmospheric Deposition Program in United States; Beachley et al., 2016) and EANET (Acid Deposition Monitoring Network in East Asia; Totsuka et al., 2005). Attributed mainly to the bias in emission data and incomplete chemical schemes, the uncertainty from CTM was reported to reach –70%–+800% and –100%–+300% for N and S, respectively (Chang et al., 2020; Dentener et al., 2006; Nowlan et al., 2014; Tan et al., 2018; Vet et al., 2014). The inferential method calculates the deposition flux as the product of the ground-level concentration and the dry deposition rate ( $V_d$ ) of concerned species (Ban et al., 2016; Totsuka et al., 2005; Xu et al., 2019). When the spatial interpolation of concentration is conducted to fill the observation gap in space, overestimation likely occurs for the entire country, as the monitoring was mostly available in urban regions with high concentrations but much less in relatively clean rural areas (Hou et al., 2019; Lye and Tian, 2007; van Donkelaar et al., 2016; Young et al., 2016). To correct the bias from the uneven distribution of monitoring sites, simple linear or nonlinear

relationships between satellite-derived column and ground-level concentration have been developed and extended for regions without ground observation data (Jia et al., 2016; Xu et al., 2018a; Yu et al., 2019; Zhan et al., 2018). The method usually ignored the influences of meteorology, population, and vegetation coverage (an indicator of limited anthropogenic activity) on air quality, and the accuracy in concentration prediction needed further improvement. Regarding  $V_d$ , in addition, studies usually collected limited observation or simulation data from literature and mapped the parameter according to the land use type (Yu et al., 2019; Zhang et al., 2003). Insufficient knowledge of other influential factors (e.g., meteorology) and discrepancy in land use classification between studies would enhance the errors in deposition estimation.

In this work, therefore, we improved the methodology of NO<sub>2</sub> and SO<sub>2</sub> dry deposition estimation in China. We selected 2013–2018 as the research period, as the country started the National Action Plan on the Prevention and Control of Air Pollution (NAPPCAP) in 2013 (van der A et al., 2017; Zhang et al., 2019). The action has resulted in great changes in emissions and air quality (Zhang et al., 2019; Zheng et al., 2018), while little information has been reported on the spatiotemporal variability of dry deposition or its driving factors. Such research gap prevented correctly understanding the effectiveness of pollution control on ecological risk. We developed a random forest (RF) algorithm to predict the NO<sub>2</sub> and SO<sub>2</sub> concentrations across the country, and applied a state-of-art global transport model to estimate the  $V_d$ . The monthly dry deposition flux was then calculated and the spatial pattern of dry deposition was explored. As far as we know, it is one of the first studies revealing the effectiveness of China's recent actions of air pollution control on the variability of dry deposition of gaseous pollutants at the national scale.

## 2. Data and methods

### 2.1. The research area

We selected mainland China as the research area including 31 provincial administrative regions. As shown in Fig. 1, the 31 provinces were geographically classified into 6 parts, i.e., Northwest (NW), Northeast (NE), North-central (NC), Southeast (SE), Southwest (SW), and the Tibetan Plateau (TP).

We also defined the four typical economically developed regions (Jing-Jin-Ji (JJJ), Yangtze River Delta (YRD), Pearl River Delta (PRD), and Sichuan-Chongqing Basin (SCB)). In the past decades, China's development plans have increasingly focused on developing urban agglomerations where economic ties and industries are concentrated. Located along the east coast of China, JJJ, YRD and PRD are the three urban agglomerations with the most active economies in China (Xing et al., 2018). They occupy 3.6% of the national land area but contain over 16% and 40% of the country's population and GDP, respectively (NBS, 2018). Located in inland China, SCB accounts for 2.0% of the national land area, 6% of the total population and 5% of the national economy (NBS, 2018). It connects SE, SW and NW China and accelerates the development of central and western regions (Zhang et al., 2020). With rapid urbanization and huge fossil energy consumption, increasing attentions have been paid to the four regions for air pollution control and emission reduction (Ma et al., 2020; Tao et al., 2017).

### 2.2. Dry deposition flux estimation

The dry deposition flux ( $F_d$ ) was calculated as the product of the predicted concentration of air pollutants ( $C$ ) and modeled dry deposition rates ( $V_d$ ):

$$F_d = C \times V_d \quad (1)$$

The spatial distribution of monthly mean concentrations of NO<sub>2</sub> and SO<sub>2</sub> were obtained at the horizontal resolution of 0.25° × 0.25°, based

on a RF model that developed the relationships between the tropospheric vertical columns densities (VCD) from satellite observation and ground-level concentrations (as will be described in Section 2.3). The daily  $V_d$  was calculated with the Goddard Earth Observation System-Chemistry (GEOS-Chem) 3-D global transport model (<http://geos-chem.org>; Bey et al., 2001) and averaged at monthly level. We used a nested version of GEOS-Chem with the native horizontal resolution of  $0.25^\circ \times 0.3125^\circ$  over East Asia ( $70\text{--}150^\circ\text{E}$ ,  $11^\circ\text{S}\text{--}55^\circ\text{N}$ ) and  $4^\circ \times 5^\circ$  for rest of the world (Zhang et al., 2016). The model assimilated meteorological field from the Goddard Earth Observation System (GEOS) of NASA Global Modeling and Assimilation Office (GMAO), with a 3 h temporal resolution (1 h for surface variables and mixing depths) at 72 levels. The calculation of dry deposition was based on a standard big-leaf resistance-in-series parameterization (Wesely, 1989).

$$V_d = (R_a + R_b + R_c)^{-1} \tag{2}$$

where  $R_a$  is aerodynamic resistance of underlying surface, which refers to the air resistance experienced by the gas from the atmosphere to the surface turbulent motion (same value for both species, Hicks et al., 1987);  $R_b$  is the quasi-laminar boundary layer resistance, which refers to the resistance of the gas from the quasi-laminar boundary layer to the near ground (Walcek et al., 1986); and  $R_c$  is the surface resistance, which refers to the resistance of gas molecules absorbed by the surface.

### 2.3. Random forest (RF) model

#### 2.3.1. Model development

RF is a statistical method to develop the complicated linear or nonlinear relationship between response variable and interpretation variables. With the ensemble learning, the RF result is determined as the arithmetic mean of the multiple decision trees (Breiman, 2001). In addition, the model provides the relative importance of variables (RIV, dimensionless) to identify the key factors (see the details in the text section in the supplement). The algorithm was of satisfying accuracy and generalization performance for the multi-layer random process applied. We ran the RF modeling program by using the “randomforest” package in R software (version 3.6.1).

Following Zhan et al. (2018), we selected satellite-derived VCDs, Normalized Difference Vegetation Index (NDVI) and meteorological factors as interpretation variables, and the response variable was the observed ground-level concentration, as summarized in Table S1 in the supplement. The spatial distributions of monthly  $\text{NO}_2$  and  $\text{SO}_2$  concentrations across the country for 2013–2018 were predicted at the horizontal resolution of  $0.25^\circ \times 0.25^\circ$ , and the robustness of RF model was tested by 10-fold cross validation. We split the entire model fitting dataset into 10 groups by year. In each round of cross validation, the samples in 9 groups were used as the training data, and the remaining

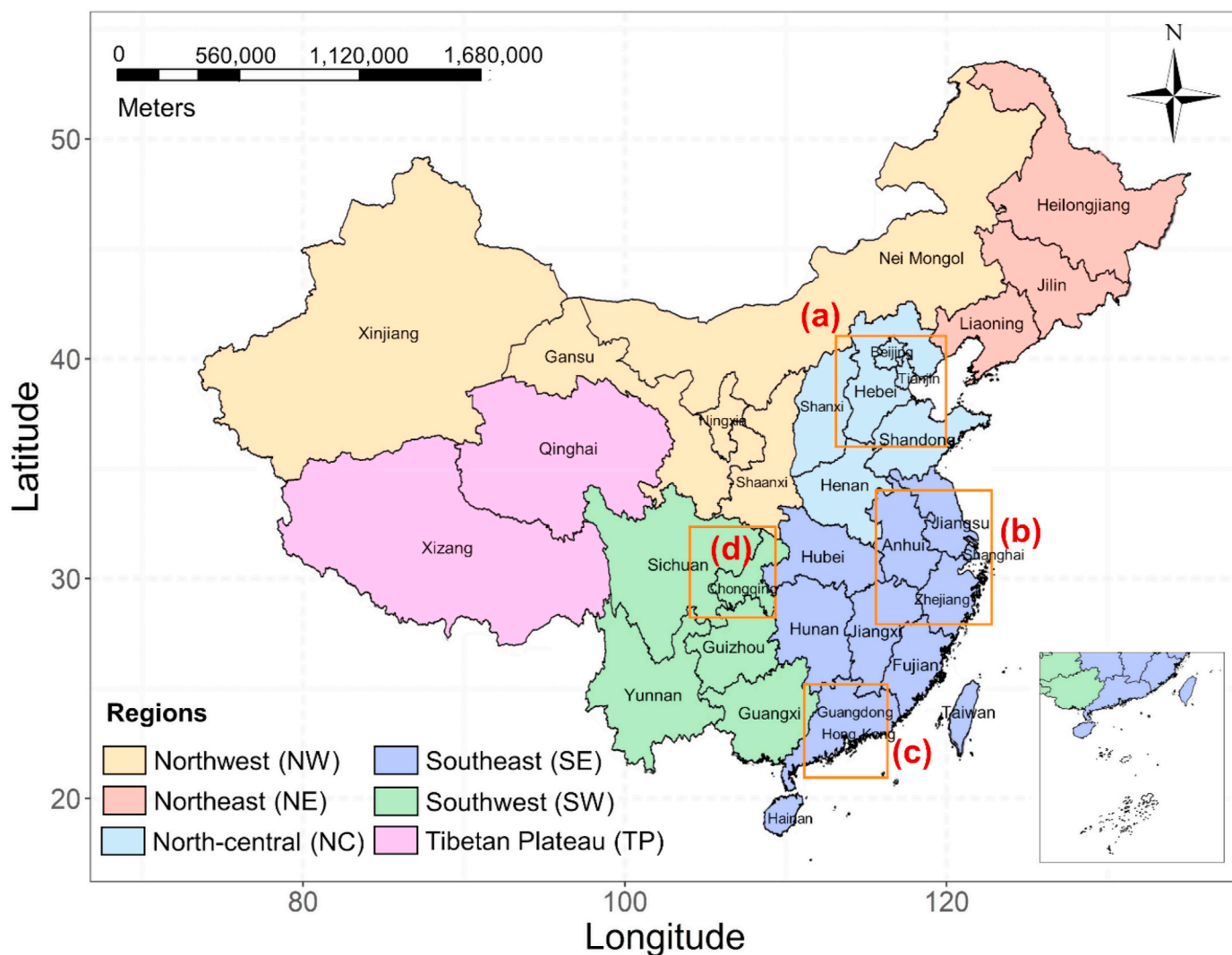


Fig. 1. The research domain of this study. The orange boxes represent JJJ (a), YRD (b), PRD (c) and SCB (d). (For interpretation of the references to colour in this figure legend, the reader is referred to the Web version of this article.)

group was applied for prediction. This process repeated 10 times and every group was tested. The consistency between the ground measurements and predictions was evaluated using statistical indicators, including coefficient of determination ( $R^2$ ), root mean squared prediction error (RMSE), mean prediction error (MPE) and relative prediction error (RPE).

To match the horizontal resolution of  $V_d$ , the  $\text{NO}_2$  and  $\text{SO}_2$  concentrations estimated from RF was re-gridded at  $0.25^\circ \times 0.3125^\circ$  to obtain the spatial pattern of dry deposition.

### 2.3.2. Data source and processing

The daily ground-level concentrations of  $\text{NO}_2$  and  $\text{SO}_2$  were obtained from the real-time data publishing system of the China National Environmental Monitoring Centre (CNEMC, <http://datacenter.mee.gov.cn/websjzx/queryIndex.vm>), with the abnormal values eliminated. The total site number increased from 834 in 2013 to 1529 in 2018. The tropospheric VCDs of  $\text{NO}_2$  from 2013 to 2018 were originated from the POMINO v2 dataset of Ozone Monitoring Instrument (OMI) level-3  $\text{NO}_2$  tropospheric product of Peking University (<http://www.temis.nl/airpollution/no2.html>) (Chatzidiakou et al., 2019; Lin et al., 2014). The algorithm was based on the LIDORT-driven AMFv6 package (Chatzidiakou et al., 2019). The VCDs with cloud coverage over 25% were eliminated as high cloudiness would distort satellite detection and increase inversion error. The daily  $\text{SO}_2$  VCDs was obtained from Level-3e OMSO2 Data Products ([https://disc.gsfc.nasa.gov/datasets/OMSO2e\\_003/summary](https://disc.gsfc.nasa.gov/datasets/OMSO2e_003/summary)). All the OMI  $\text{SO}_2$  data were generated by an algorithm based on principal component analysis (PCA), which was considerably sensitive to anthropogenic emissions (Krotkov et al., 2015). The exclusion of abnormal values followed 13 criteria, containing observation time, local calendar date, radiative cloud fraction, solar zenith angle, solar eclipse possibility flag set and row anomaly flag set ([https://acdisc.gesdisc.eosdis.nasa.gov/data/Aura\\_OMI\\_Level3/OMSO2e.003/doc/README.OMSO2e.pdf](https://acdisc.gesdisc.eosdis.nasa.gov/data/Aura_OMI_Level3/OMSO2e.003/doc/README.OMSO2e.pdf)). Monthly mean VCDs of  $\text{NO}_2$  and  $\text{SO}_2$  were calculated based on the daily product from 2013 to 2018. We used the Kriging interpolation method to fill the missing values, and developed the spatial patterns of VCDs at the horizontal resolution of  $0.25^\circ \times 0.25^\circ$ .

For NDVI, we selected the monthly interval data from the 13Q1 series of Moderate Resolution Imaging Spectroradiometer (MODIS) Level-3 product at  $0.1^\circ \times 0.1^\circ$  ([https://neo.sci.gsfc.nasa.gov/archive/csv/MOD\\_NDVI\\_M/](https://neo.sci.gsfc.nasa.gov/archive/csv/MOD_NDVI_M/)). The vegetation index equations used the red and near-infrared reflectance signals to separate and strengthen the green and photosynthetic active vegetation components. The red and near-infrared responses were processed by radiometric, cloud filtering, atmospheric correction, spatiotemporal gridding and perspective adjustment to generate a Level 3 vegetation index map ([https://eosps0.gsfc.nasa.gov/sites/default/files/atbd/atbd\\_mod13.pdf](https://eosps0.gsfc.nasa.gov/sites/default/files/atbd/atbd_mod13.pdf)). The numerical value of NDVI >1 was assigned to vacancy value (NA).

The meteorological parameters included rainfall data, boundary layer height, wind speed, wind pressure, temperature at 2 m, wind direction, cloud water, total column ozone, and total water volume (Table S1). The monthly precipitation data from 2013 to 2018 at 2160 ground observation stations were obtained from China Meteorological Administration (<http://data.cma.cn/data/cdcdetail/dataCode/>). The monthly means of other meteorological parameters were downloaded from the European Centre for Medium-Range Weather Forecasts (ECMWF, [https://apps.ecmwf.int/datasets/data/interim-full-daily/levt\\_ypr=sfc/](https://apps.ecmwf.int/datasets/data/interim-full-daily/levt_ypr=sfc/)) at the resolution of  $0.25^\circ \times 0.25^\circ$ .

## 3. Results and discussions

### 3.1. The predicted ground-level concentrations of $\text{NO}_2$ and $\text{SO}_2$

#### 3.1.1. Model performance and variable contribution to the prediction

The RF model performances with 10-fold cross validation are shown in Fig. S1 and S2 in the supplement for  $\text{NO}_2$  and  $\text{SO}_2$ , respectively. The

annual mean  $R^2$  of  $\text{NO}_2$  and  $\text{SO}_2$  were above 0.62 and 0.71, respectively, indicating the satisfying correlations between observation and prediction. Improved model performance was found along with the growth of monitoring station numbers in the RF model, indicated by the elevated  $R^2$  and reduced RMSE, MPE and RPE. For  $\text{NO}_2$ , as an example, the  $R^2$  increased from 0.62 in 2013 to 0.75 in 2018, and the RMSE and RPE decreased from  $6.36$  to  $5.57 \mu\text{g m}^{-3}$  and from 36.1% to 18.2%, respectively (Fig. S1). Increased ground-level stations are expected to expand the spatial coverage and to improve the spatial distribution of air pollutant observation, and thus could help reduce the uncertainty of the RF model. Due to the gradual implementation of quality assurance/quality control techniques in observation, moreover, the better ground-level concentration data in more recent years could be another reason for the improved model performance.

Fig. S3 summarizes the RIV of interpretation variables to the predictions in RF models. VCDs were found to be of the greatest impact on ground-level concentration prediction, with the RIV estimated at 15.9 for  $\text{NO}_2$  and 11.8 for  $\text{SO}_2$ . Complex relationships between response variables and interpretation variables were revealed as shown in Fig. S4 in the supplement. There was a positive correlation between VCDs and the ground-level concentrations within a certain range. The  $\text{NO}_2$  concentration increased almost linearly from 22 to  $40 \mu\text{g m}^{-3}$  when the VCD was elevated from  $1 \times 10^{15}$  to  $16 \times 10^{15}$  molec./ $\text{cm}^2$  (Fig. S4a). When VCD exceeded  $16 \times 10^{15}$  molec./ $\text{cm}^2$  for  $\text{NO}_2$ , its influence on ground-level concentration prediction became limited and smaller than that of other variables (such as meteorology and land use). Similar situation was found for  $\text{SO}_2$ , with the threshold of VCD at  $0.7 \times 10^{15}$  molec./ $\text{cm}^2$  (Fig. S4b). Great impact was also identified from meteorological parameters including wind speed at 10 m, PBLH, wind direction, temperature at 2 m, surface pressure and precipitation, with their total importance value aggregated at 74.6 and 80.2 for  $\text{NO}_2$  and  $\text{SO}_2$ , respectively. As the most important meteorological variable, wind speed ('si10' in Fig. S3) exhibited negative effect on ground-level concentrations (Fig. S4), since high wind speed was more conducive to the diffusion and removal of pollutants. Low temperature was often associated with low PBLH, resulting in air stagnation and condensation of gaseous pollutants near the ground. Rainfall had a relatively high negative impact on  $\text{SO}_2$  (with RIV at 8.9), as  $\text{SO}_2$  was easily soluble in water and would be converted into sulfate with abundant rainfalls. In addition, relatively high NDVI that represented few human activities limited the anthropogenic emissions, and the concentrations of  $\text{NO}_2$  and  $\text{SO}_2$  were reduced accordingly.

#### 3.1.2. Spatial and temporal variations of predicted ground-level concentrations

Table 1 summarizes the seasonal means of the predicted  $\text{NO}_2$  and  $\text{SO}_2$  concentrations during 2013–2018, and Fig. S5 in the supplement illustrates the monthly variations of concentrations. The highest concentrations were found in December and January and the lowest in July and August. The average  $\text{NO}_2$  concentration in winter ( $31.7 \mu\text{g m}^{-3}$ ) was nearly twice of that in summer ( $18.2 \mu\text{g m}^{-3}$ ), and the average  $\text{SO}_2$  concentration in winter ( $38.6 \mu\text{g m}^{-3}$ ) was much higher than that in other seasons. This seasonal pattern resulted mainly from the dual influences of anthropogenic emissions and meteorology (Kang et al., 2019; Kuerban et al., 2020; Liu et al., 2018a; Tian et al., 2019; Wang et al., 2019). Elevated  $\text{NO}_x$  and  $\text{SO}_2$  emissions resulted from the increased coal burning for heating in winter, particularly in the north. Unfavorable meteorological conditions (e.g., low PBLH and temperature, high atmospheric pressure, low precipitation and wind speed) prevailed in winter, and the weak diffusion and chemical reactivity enhanced the accumulation of air pollutants in the atmosphere. In contrast, the stronger atmospheric turbulence and photochemical activity of  $\cdot\text{OH}$  accelerated the diffusion and chemical conversion of  $\text{NO}_2$  and  $\text{SO}_2$ , and thereby decreased the concentrations (Fan et al., 2020; Kuerban et al., 2020).

As presented in Tables 2 and 3, the national annual averages of  $\text{NO}_2$

**Table 1**

The seasonal means of the predicted ground-level concentration ( $C$ ), dry deposition rate ( $V_d$ ) and dry deposition flux ( $F_d$ ) for mainland China during 2013–2018.

	$C$ ( $\mu\text{g m}^{-3}$ )		$V_d$ ( $\text{cm s}^{-1}$ )		$F_d$ ( $\text{kgN/S ha}^{-1}$ )	
	$\text{NO}_2$	$\text{SO}_2$	$\text{NO}_2$	$\text{SO}_2$	$\text{NO}_2$	$\text{SO}_2$
Spring	23.90 ± 0.05	21.52 ± 0.06	0.09	0.53	0.60 ± 0.06	2.93 ± 0.10
Summer	18.22 ± 0.03	14.64 ± 0.03	0.18	0.62	0.91 ± 0.05	2.48 ± 0.10
Autumn	26.01 ± 0.06	21.55 ± 0.06	0.11	0.60	0.73 ± 0.04	3.07 ± 0.10
Winter	31.68 ± 0.08	38.60 ± 0.14	0.05	0.57	0.31 ± 0.04	4.48 ± 0.09

Note: The seasonal mean of  $C$  and  $V_d$  was calculated by the arithmetic average of monthly datasets. The  $F_d$  was the sum of the monthly data. The standard error of mean (s.e.) of monthly data was calculated as  $sd/\sqrt{n}$ , where  $sd$  is the standard deviation.

and  $\text{SO}_2$  concentrations ranged 20.1–32.0 and 14.0–32.8  $\mu\text{g m}^{-3}$  during 2013–2018, respectively. Significant declining trends ( $p < 0.001$ ) were found for both species, with the annual decreasing rates calculated at 1.9 and 4.6  $\mu\text{g m}^{-3} \text{ yr}^{-1}$  for  $\text{NO}_2$  and  $\text{SO}_2$ , respectively (Fig. S6 in the Supplement). The measures of NAPPAP were believed to contribute greatly to the reduced concentrations (Ebenstein et al., 2017; Tian et al., 2019). Those measures included elevated implementations of flue gas desulfurization (FGD) and selective catalytic reduction (SCR) systems on power boilers, sintering furnaces, and cement precalciners, and promotion of clean energy in industrial, traffic and residential sources. Consequently, the national  $\text{NO}_x$  and  $\text{SO}_2$  emissions were estimated to decline 20% and 59% from 2013 to 2017 by the Multi-resolution Emission Inventory for China (MEIC, <http://meicmodel.org/>), and the corresponding reductions in concentrations were estimated at 29% and 45% (indicated in Tables 2 and 3), respectively (Zheng et al., 2018). As  $\text{SO}_2$  comes mainly from coal combustion while  $\text{NO}_x$  is from more complicated sources categories, the much larger reduction in  $\text{SO}_2$  than  $\text{NO}_2$  during the research period reflected the bigger success in  $\text{SO}_2$  emission control through earlier and better operation of FGD systems on coal-fired boilers.

Fig. S7 in the Supplement illustrates the spatial patterns of predicted annual  $\text{NO}_2$  concentrations for 2013–2018. Higher concentrations were

found east to the Hu-Line (a commonly used northeast-to-southwest geographical division of China separating areas with different climates and topographies) than the west, attributed to larger densities of population and industrial economy in the east. In particular, the hotspots of  $\text{NO}_2$  concentrations include NC, north of SE, and the four typical regions, resulting basically from the relatively high emissions of anthropogenic origin in those regions (Li, 2020; van der A et al., 2017). In general, the more urbanization and industrialization in the east of the country resulted in abundant fossil fuel consumption and intensive traffic, and the emission intensities were clearly larger than the west (see the regional emission intensities in Table 2).

The biggest relative reduction in  $\text{NO}_2$  concentration from 2013 to 2018 was found for TP at  $-42.4\%$ , followed by NE ( $-36.6\%$ ), NW ( $-29.2\%$ ), SW ( $-26.6\%$ ), SE ( $-17.9\%$ ) and NC ( $-10.2\%$ ). Faster concentration declines in the west than in the east were consistent with the pattern of anthropogenic emissions (Table 2). Although SCR has been used in specific sectors (e.g., power generation and cement production) to limit the  $\text{NO}_x$  emissions, this measure was insufficient for the industrial boilers which accounted for the largest fraction of emissions (Liu et al., 2016; Zheng et al., 2018). Furthermore, fast urbanization and industrialization and the swift growth in vehicles and newly-built industrial plants in eastern provinces partly weakened the effect of air pollution control measures on emission abatement (Ding et al., 2017; Wu et al., 2017; Xu et al., 2018c). The possible large uncertainty in the prediction of  $\text{NO}_2$  concentrations in the west, due to relatively rare ground-level observation stations and the potentially high bias of satellite observation in relatively clean areas should be noted as well.

Fig. S8 in the supplement shows the spatial pattern of  $\text{SO}_2$  concentration by year. Taking the Qinling-Huaihe Line as the boundary, the concentration in the north was higher than that in the south, particularly in central NC, south of NE, and south of NW.  $\text{SO}_2$  was mainly emitted from coal burning, and it can be easily oxidized into  $\text{SO}_3$  through gas-phase or aqueous pathways, with a lifetime of  $\sim 1$  week and a short transport distance (Chen et al., 2018; Engardt et al., 2005; Hung and Hoffmann, 2015; Lin et al., 2008; Park, 2004; Zhang et al., 2021b). Therefore, the high concentration implied abundance of large coal-fired power plants and industrial boilers in the north (Liu et al., 2019; Wang et al., 2020; Zhao et al., 2019). From 2013 to 2018, the relative reduction in  $\text{SO}_2$  concentration in the north was commonly larger than that in the south. As shown in Table 3, the concentrations in NC and NE were

**Table 2**

The emissions ( $E$ ), ground-level concentrations ( $C$ ) and dry deposition flux ( $F_d$ ) of  $\text{NO}_2$  for China and the six regions from 2013 to 2018. The emission data were taken from the Multi-resolution Emission Inventory for China (MEIC, <http://meicmodel.org/>).

	Regions	2013	2014	2015	2016	2017	2018	Relative change <sup>1</sup>
$E$ ( $\text{kgN ha}^{-1} \text{ yr}^{-1}$ )	NC	72.8	67.6	60.3	58.2	57.3	–	$-21.3\%$
	NE	21.1	20.4	19.4	18.9	18.5	–	$-12.5\%$
	NW	10.0	9.4	9.1	8.5	8.7	–	$-13.5\%$
	SE	48.4	43.9	42.6	41.2	41.1	–	$-15.1\%$
	SW	12.9	11.6	10.9	10.0	9.6	–	$-25.8\%$
	TP	1.7	1.6	1.4	1.3	1.2	–	$-26.9\%$
	China	12.3	11.3	10.6	10.1	9.8	–	$-20.4\%$
	$C$ ( $\mu\text{g NO}_2 \text{ m}^{-3}$ )	NC	39.4	39.4	36.4	37.1	38.6	35.4
NE		34.8	31.6	25.6	24.3	24.4	22.1	$-36.6\%$
NW		32.5	30.2	22.7	23.6	25.9	23.0	$-29.2\%$
SE		29.9	28.4	24.8	24.9	26.2	24.5	$-17.9\%$
SW		27.6	27.5	20.5	20.2	21.6	20.2	$-26.6\%$
TP		25.4	27.1	16.7	17.1	18.0	14.6	$-42.4\%$
China		32.0	27.5	21.6	21.5	22.9	20.1	$-37.1\%$
$F_d$ ( $\text{kgN ha}^{-1} \text{ yr}^{-1}$ )		NC	4.5	4.7	4.3	4.4	4.5	4.1
	NE	5.0	4.9	3.8	3.8	3.7	3.4	$-33.3\%$
	NW	2.1	2.1	1.6	1.6	1.7	1.5	$-30.6\%$
	SE	5.5	5.4	4.5	4.5	4.7	4.2	$-24.4\%$
	SW	5.3	5.3	3.9	3.7	4.0	3.5	$-33.2\%$
	TP	1.2	1.3	0.9	0.9	0.9	0.7	$-38.9\%$
	China	3.1	3.0	2.3	2.3	2.4	2.1	$-32.3\%$

<sup>1</sup>Note: The change of 2018 relative to 2013 for  $C$  and  $F_d$ , and that of 2017 relative to 2013 for  $E$  as the emission data for 2018 were unavailable when this work was conducted.

**Table 3**The same as Table 2 but for SO<sub>2</sub>.

	Regions	2013	2014	2015	2016	2017	2018	Relative change <sup>1</sup>
<i>E</i> (kgN ha <sup>-1</sup> yr <sup>-1</sup> )	NC	80.4	62.8	47.0	35.8	29.5	–	–63.3%
	NE	16.1	14.5	12.0	9.9	7.9	–	–51.0%
	NW	21.3	19.1	16.0	12.3	10.1	–	–52.4%
	SE	27.5	21.1	18.1	14.8	11.6	–	–57.8%
	SW	29.8	23.2	18.7	14.1	11.0	–	–63.0%
	TP	1.3	1.1	1.0	0.7	0.6	–	–52.0%
	China	12.7	10.2	8.5	6.7	5.3	–	–58.5%
<i>C</i> (µg NO <sub>2</sub> m <sup>-3</sup> )	NC	46.9	44.5	34.5	29.5	23.9	16.6	–64.7%
	NE	40.6	38.3	27.0	23.4	19.8	14.8	–63.5%
	NW	41.0	39.6	27.3	24.9	22.1	16.5	–59.8%
	SE	23.9	22.7	17.0	14.5	12.5	10.1	–57.7%
	SW	25.5	25.5	16.3	14.2	12.6	10.8	–57.6%
	TP	28.1	28.9	21.4	18.9	17.3	12.5	–55.4%
	China	32.8	34.1	23.4	20.4	17.9	14.0	–57.4%
<i>F<sub>d</sub></i> (kgN ha <sup>-1</sup> yr <sup>-1</sup> )	NC	26.5	25.0	19.6	16.8	13.6	9.5	–64.0%
	NE	21.1	21.2	14.9	13.2	11.1	8.6	–59.4%
	NW	20.3	19.9	13.6	12.4	11.0	8.3	–59.2%
	SE	18.5	17.1	13.4	11.7	10.2	8.2	–55.9%
	SW	16.7	16.9	11.0	9.5	8.4	7.1	–57.7%
	TP	13.4	14.2	10.5	9.3	8.2	5.9	–56.0%
	China	18.4	18.2	12.7	11.3	9.8	7.5	–59.2%

<sup>1</sup>Note: The change of 2018 relative to 2013 for *C* and *F<sub>d</sub>*, and that of 2017 relative to 2013 for *E* as the emission data for 2018 were unavailable when this work was conducted.

estimated to decline over 63%, while those in SE and SW around 58%. Similarly, substantial emission abatement was reported for all the six regions in MEIC, particularly for NC at 63%. On one hand, tightened emission standards and strict emission control measures have been gradually applied on a great number of coal-fired boilers in the north. On the other hand, the coal consumption for household heating in winter has been partly replaced by natural gas or electricity in the rural north regions (China, 2018; Wang et al., 2020). Those efforts proved effective in restraining SO<sub>2</sub> emissions and thereby reducing the ground-level concentrations.

### 3.2. The simulated dry deposition rate (*V<sub>d</sub>*) of NO<sub>2</sub> and SO<sub>2</sub>

The national annual mean *V<sub>d</sub>* was simulated at 0.11 and 0.58 cm s<sup>-1</sup> for NO<sub>2</sub> and SO<sub>2</sub>, respectively (Table S2 in the supplement), with nearly no inter-annual change during the research period. The differences between this work and other available simulation studies ranged from –64% to 27% for NO<sub>2</sub> and from –40% to 5% for SO<sub>2</sub> (Su et al., 2012; Xu et al., 2015; Yu et al., 2019; Zhang et al., 2003, 2004). The considerable differences in the estimated *V<sub>d</sub>* largely reflect uncertainties in the model parameterizations and its high sensitivity to some inputs such as land type and near-surface meteorological variables used in the model (Chang et al., 2020; Flechard et al., 2011; Jia et al., 2016; Lu et al., 2020). Despite some uncertainties in the *V<sub>d</sub>* estimation and the lack of direct *V<sub>d</sub>* observations, the method has been proven to be valid. For example, nitrogen deposition fluxes in China have been previously estimated based on surface concentration measurements and *V<sub>d</sub>* using the GEOS-Chem model (Zhao et al., 2017).

Fig. S9 in the supplement illustrates the difference in monthly variation of *V<sub>d</sub>* for the two species. The NO<sub>2</sub> *V<sub>d</sub>* was the highest in summer (0.18 cm s<sup>-1</sup>, Table 1) and the lowest in winter (0.05 cm s<sup>-1</sup>), while the seasonal variation for SO<sub>2</sub> was smaller, with the highest in summer (0.62 cm s<sup>-1</sup>) and the lowest in spring (0.53 cm s<sup>-1</sup>). The seasonal variation of *V<sub>d</sub>* could depend on underlying surface condition and meteorological factors (Zhao et al., 2015; Zhou et al., 2010). As NO<sub>2</sub> is insoluble in water with a small Henry coefficient, *R<sub>c</sub>* was much larger than other resistance factors and dominated the seasonal variation of *V<sub>d</sub>* (Zhang et al., 2004; Zhou et al., 2010). Given that *R<sub>c</sub>* represents the resistance of gas absorbed by surface, the seasonal variation of underlying surface could play an important role on that of *V<sub>d</sub>*. In summer with abundant solar radiation and vegetation, the stomatal opening degree of

leaf was larger on the surface, which helped removal of atmospheric NO<sub>2</sub> and elevated the *V<sub>d</sub>*. The vegetation cover decreased sharply in winter, resulting in the lowest *V<sub>d</sub>*. For SO<sub>2</sub> that is more soluble in water with a larger Henry coefficient, the magnitude of *R<sub>c</sub>* was similar to that of *R<sub>a</sub>* and *R<sub>b</sub>*, and all the three resistance factors contributed to the seasonal variation of *V<sub>d</sub>*. In particular, the higher temperature in summer and autumn led to the stronger gas turbulence and decreased *R<sub>a</sub>* and *R<sub>b</sub>*. Besides solar radiation that could influence the opening and closing of the stomata and thereby *R<sub>c</sub>* as mentioned above, high humidity and adequate precipitation would also reduce *R<sub>c</sub>* through elevated absorption of SO<sub>2</sub> by canopy, especially in the summer rainy season. Different from NO<sub>2</sub>, there was a peak of SO<sub>2</sub> *V<sub>d</sub>* in winter. More snow cover in winter may behave as water (with high *V<sub>d</sub>*, Tables S2 and S3) so that dry deposition is enhanced (Zhang et al., 2004).

Fig. S10 in the Supplement shows the spatial distribution of the modeled *V<sub>d</sub>* for NO<sub>2</sub> and SO<sub>2</sub>, and larger *V<sub>d</sub>* was commonly found in the east and the south of the country. As summarized in Table S3 in the supplement, clear difference existed in *V<sub>d</sub>* for various types of underlying surfaces, thus the geographical distribution of land use categories directly explained the spatial pattern of *V<sub>d</sub>*. NO<sub>2</sub> was easily adsorbed to the vegetation surface, thus higher *V<sub>d</sub>* was in particular found for the forestland, sparse forestland, and shrub forest in SE and SW. For SO<sub>2</sub> with strong absorption capacity by water, *V<sub>d</sub>* was largest for tidal-flat, ocean, and reservoir pond, followed by vegetation. In general, the *V<sub>d</sub>* in areas with high air humidity and more vegetation was much higher than that in arid areas for both gases. The larger *V<sub>d</sub>* of vegetation surface than other types (except for SO<sub>2</sub> of water surface) helped explain the low ground-level concentration in the region with high NDVI as stated in Section 3.1, besides the limited anthropogenic emissions.

### 3.3. Temporal and spatial patterns of dry deposition

#### 3.3.1. NO<sub>2</sub> dry deposition

The orange line in Fig. 2 indicates the monthly variation of NO<sub>2</sub> dry deposition during 2013–2018 (see the seasonal means in Table 1). The highest dry deposition was found in summer and the lowest in winter. This seasonal fluctuation resembled that of *V<sub>d</sub>*, which was nearly 4 times higher in summer. Despite of the higher emissions and concentration in winter, meteorology and vegetation limited the *V<sub>d</sub>* and inhibited the dry deposition.

Fig. 3a illustrates the time series and inter-annual variability of NO<sub>2</sub>

dry deposition from 2013 to 2018 (see the annual means in Table 2). The nationwide dry deposition was estimated to decline from 3.1 to 2.1 kg N ha<sup>-1</sup> yr<sup>-1</sup>, with the annual reduction rate estimated at 0.21 kg N ha<sup>-1</sup> yr<sup>-1</sup> ( $p < 0.001$ ). The reduction reflected the benefit of the NAPCCAP measures on emissions for the whole country, e.g., the expanded use of SCR on power plants and cement kilns. The relative reduction in the national NO<sub>x</sub> emissions was estimated at 20% from 2013 to 2017 (Zheng et al., 2018), very close to that in NO<sub>2</sub> dry deposition at 23% (as indicated by  $F_d$  for China for 2013 and 2017 in Table 2). In particular, both the power and cement production sectors cut over 45% of their emissions, driving the total emission reduction for the country (Liu et al., 2018b; Zheng et al., 2018).

Fig. 4 presents the spatial pattern of NO<sub>2</sub> dry deposition across the country by year. Similar with concentration, the NO<sub>2</sub> dry deposition in the regions east to the Hu-Line (e.g., NC and SE) was commonly higher than those west (e.g., NW and TP), resulting mainly from the large fossil fuel consumption and emission intensity. The hotspots include Fujian, Yunnan, Zhejiang and Guangdong, attributed mainly to the very high abundance of vegetation and thereby large  $V_d$  in those subtropical provinces. As shown in Fig. S11 in the Supplement, the ratios of annual dry deposition to emissions were around 10% or smaller for NC and SE, indicating the limited deposition received in those two regions compared to their high emissions (note this current analysis does not include another significant species of oxidized nitrogen deposition, HNO<sub>3</sub>). The ratios for NE, NW and SW ranged 20–41%, and the largest ratio (72%) was found for TP. The very high ratio of dry deposition to emissions indicated that TP was strongly influenced by regional pollution transport. All the regions had their dry deposition decreased from 2013 to 2018 as shown in Table 2, and the largest relative reduction was found at 39% for TP, followed by SW (33%), NE (33%), NW (31%), SE (24%), and NC (11%). The inter-annual variation of NO<sub>2</sub> dry deposition was dominated by that of NO<sub>2</sub> concentration, and the growing industrial capacity and traffic in developed eastern regions slowed down their declines in emissions and deposition.

Fig. 5a and b presents the inter-annual changes of NO<sub>2</sub> emissions and dry deposition for the four typical economic regions in China, respectively. The largest deposition was found in PRD, followed by JJJ and YRD, and the lowest in SCB. The dry deposition in all the four regions were basically higher than the national average, while the relative reduction rates from 2013 to 2018 were estimated at 14%, 18%, 26% and 27% for JJJ, YRD, PRD and SCB, respectively, smaller than that for the whole country of 32% reduction. As mentioned earlier, the elevated

industrial capacity and traffic in the developed regions was expected to weaken the benefit of recent controls on emissions and deposition. Relatively big reduction in dry deposition was achieved for SCB, which is located in the SW with less growth of industry and thereby larger emission abatement.

### 3.3.2. SO<sub>2</sub> dry deposition

Indicated by the blue line in Fig. 2, the dry deposition of SO<sub>2</sub> was highest in winter (4.5 kg S ha<sup>-1</sup> yr<sup>-1</sup>) and lowest in summer (2.5 kg S ha<sup>-1</sup> yr<sup>-1</sup>). The seasonal variability was dominated by that of ground-level concentrations (Fig. S5), revealing the importance of emission sources to deposition. As SO<sub>2</sub> is easily soluble in water, wet deposition is likely enhanced in the more rainy summer thus reducing dry deposition in this season.

Fig. 3b shows the time series and inter-annual variability of SO<sub>2</sub> dry deposition. The annual dry deposition was estimated to continuously decline in China from 18.4 in 2013 to 7.5 kg S ha<sup>-1</sup> yr<sup>-1</sup> in 2018 (see the numbers in Table 3), with the annual reduction rate estimated at 2.4 kg S ha<sup>-1</sup> yr<sup>-1</sup> ( $p < 0.001$ ). The significant reduction in dry deposition resulted mainly from the great efforts on SO<sub>2</sub> abatement in the country. Attributed mainly to the improved operation of FGD on power and industrial sectors, the national SO<sub>2</sub> emissions were calculated in MEIC to decline 59% during 2013–2017 (Zheng et al., 2018), while the dry deposition decreased 47% as indicated by  $F_d$  for China for 2013 and 2017 in Table 3. The much larger relative reduction in both emissions and deposition of SO<sub>2</sub> than NO<sub>2</sub> implied a great success of national policy on SO<sub>2</sub> control.

Taking the Qinling-Huaihe Line as the boundary, the dry deposition of SO<sub>2</sub> in the north (NC, NW and NE) was generally higher than that in the south (SE, SW and TP), as shown in Fig. 6. The hotspots included Shanxi, Hebei, northern Henan, and western Shandong. The spatial pattern of dry deposition could be influenced both by emissions and meteorology. On one hand, as mentioned in Section 3.1, coal-fired boilers for power and heating were intensively distributed in the north, leading to abundant SO<sub>2</sub> emissions and thereby dry deposition. On the other hand, the relatively stable weather condition with less convection in the north was unfavorable to the dispersion and dilution of pollutants. The abundant emissions were thus liable to be deposited locally. In addition, the more winter snowfall in the north promoted SO<sub>2</sub> dissolution on the snow-covered surface, and thus elevated the  $V_d$ . The ratios of annual dry deposition to emissions for SO<sub>2</sub> were found to be larger than NO<sub>2</sub>, implying the easier removal of SO<sub>2</sub> from the

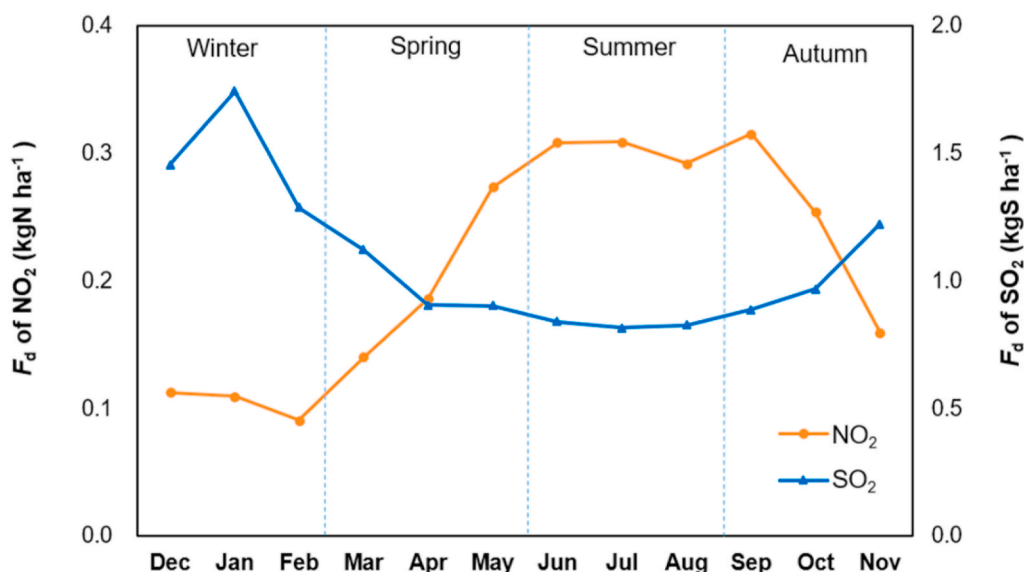
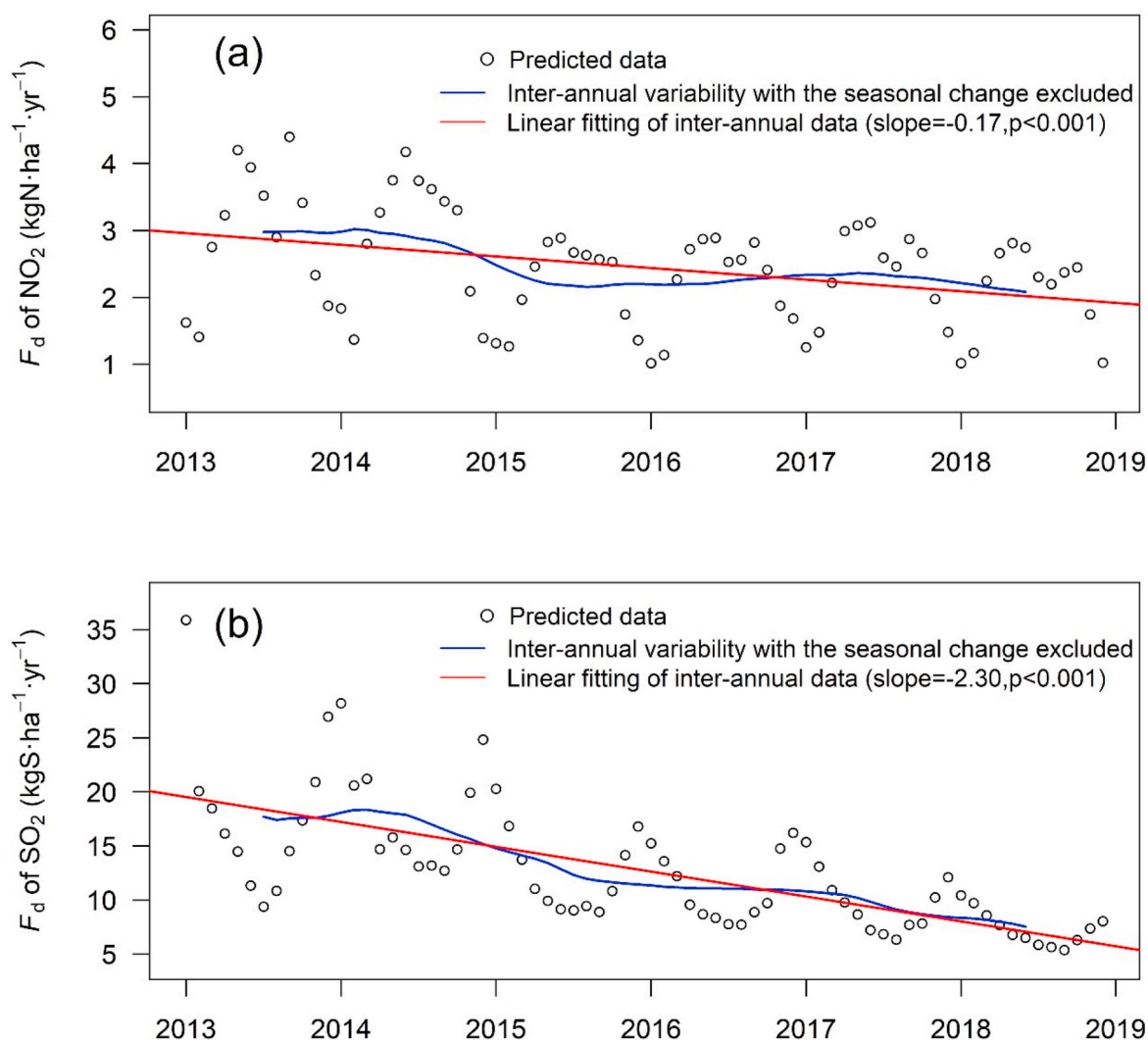


Fig. 2. The monthly means of NO<sub>2</sub> and SO<sub>2</sub> dry deposition flux ( $F_d$ ) during 2013–2018.



**Fig. 3.** The time series and inter-annual variabilities of the dry deposition flux of NO<sub>2</sub> (a) and SO<sub>2</sub> (b). The black hollow point represents the monthly dry deposition flux; the blue line represents the inter-annual variability after removing the seasonal change through time-series decomposition; and the red line represents the linear fitting of the inter-annual data. (For interpretation of the references to colour in this figure legend, the reader is referred to the Web version of this article.)

atmosphere (Fig. S11). Among the six regions, small ratios were found in relatively developed NC, SE and SW regions ranging 41–78%, while the ratios exceeded 100% for the remaining three regions, with the largest value over 1000% for TP. Similar with NO<sub>2</sub>, the much larger ratio of dry deposition to emissions for TP revealed the important role of air pollution transport to the clean plateau area in the west.

From 2013 to 2018, the dry deposition of SO<sub>2</sub> in all the six regions decreased significantly (Table 3). The largest relative reduction rate was found for NC at 64%, followed by NE (59%), NW (59%), SW (58%), TP (56%), and SE (56%). Compared to NO<sub>2</sub>, more homogeneous reduction ratios for SO<sub>2</sub> indicated the relatively consolidated implementation of SO<sub>2</sub> control measures across the country. In contrast to NO<sub>2</sub> that declined slower in regions with higher deposition, the SO<sub>2</sub> dry deposition declined faster in the regions with higher deposition values in the north of country. As mentioned earlier, multiple measures jointly resulted in successful control on SO<sub>2</sub> emissions from coal burning sources, including increased FGD use on boilers, replacement of dirty stoves with clean ones, and promotion of clean energy (e.g., electricity and natural gas) for rural heating.

Fig. 5c and d presents the inter-annual changes of SO<sub>2</sub> emissions and dry deposition for the four typical economic regions, respectively. Both the emission intensity and dry deposition in JJJ were clearly larger than other three regions, attributed mainly to the intensive coal burning

activities in the region. The relative reductions in dry deposition during 2013–2018 were calculated at 63%, 59%, 53% and 65% for JJJ, YRD, PRD and SCB, respectively. Compared to the national level at 59%, larger reduction rates were found for JJJ and SCB, almost equivalent one was found for YRD, and smaller was found for PRD. The result confirmed the effectiveness of SO<sub>2</sub> control on atmospheric dry deposition for the developed regions through NAPPAP.

#### 4. Conclusions

We present China's dry deposition of SO<sub>2</sub> and NO<sub>2</sub> during 2013–2018 combining a random forest (RF) algorithm and the GEOS-Chem model. The RF model successfully predicted the monthly ground-level concentrations of NO<sub>2</sub> and SO<sub>2</sub> at the horizontal resolution of  $0.25^\circ \times 0.25^\circ$ , with satisfying consistency with available observations. In general, high concentrations were found in winter and low in summer, and the concentrations were continuously reduced during the research period, due to the improved implementation of the national emission control measures. The annual dry deposition of NO<sub>2</sub> was ranged between 2.1 and 3.1  $\text{kg N ha}^{-1} \text{yr}^{-1}$ , with higher deposition in summer and lower in winter. The deposition east to the Hu-Line was clearly larger, particularly in North and Southeast China, while the deposition declined faster in the relatively clean TP region. The relative

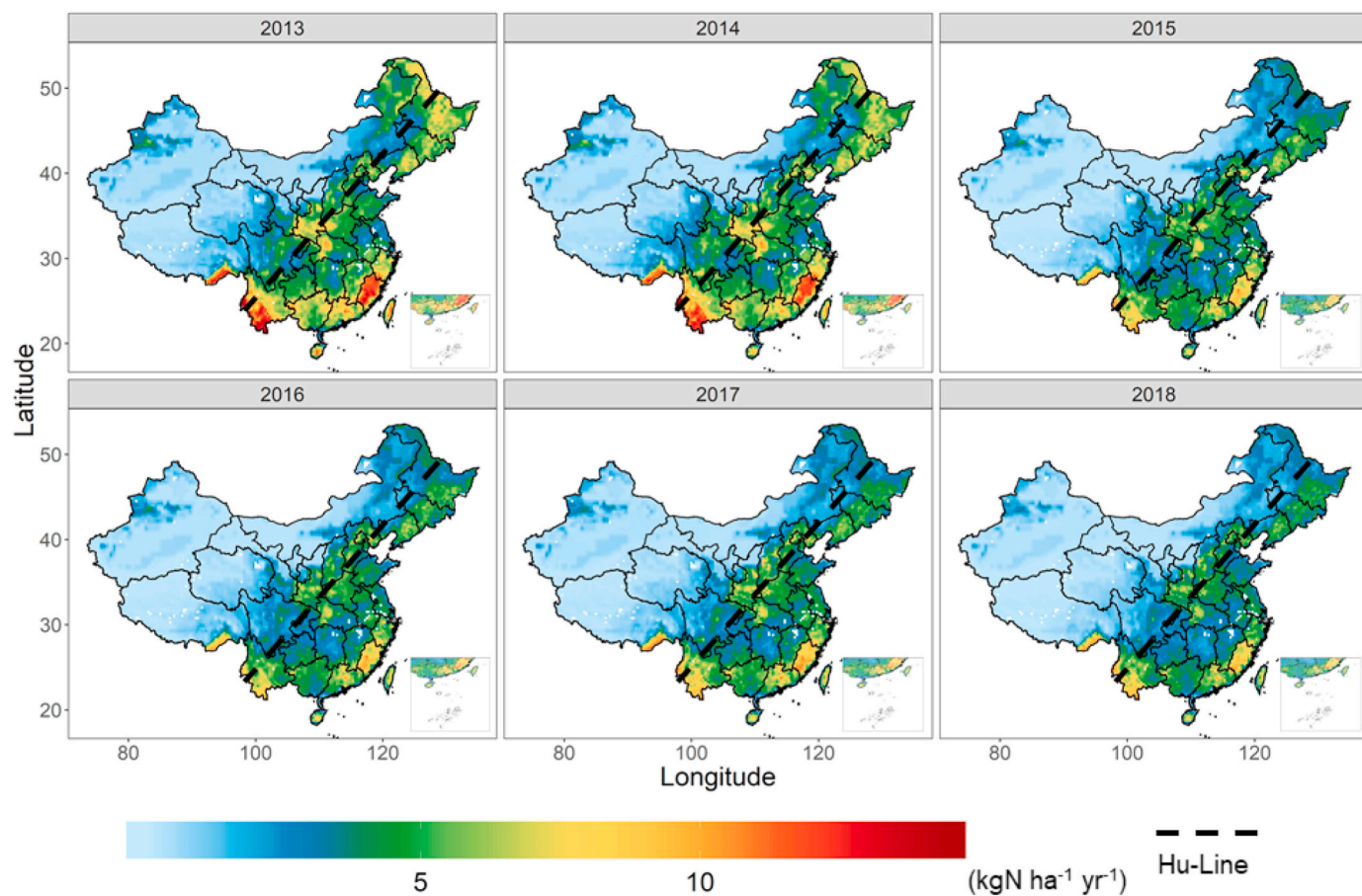


Fig. 4. The spatial distributions of NO<sub>2</sub> dry deposition flux from 2013 to 2018.

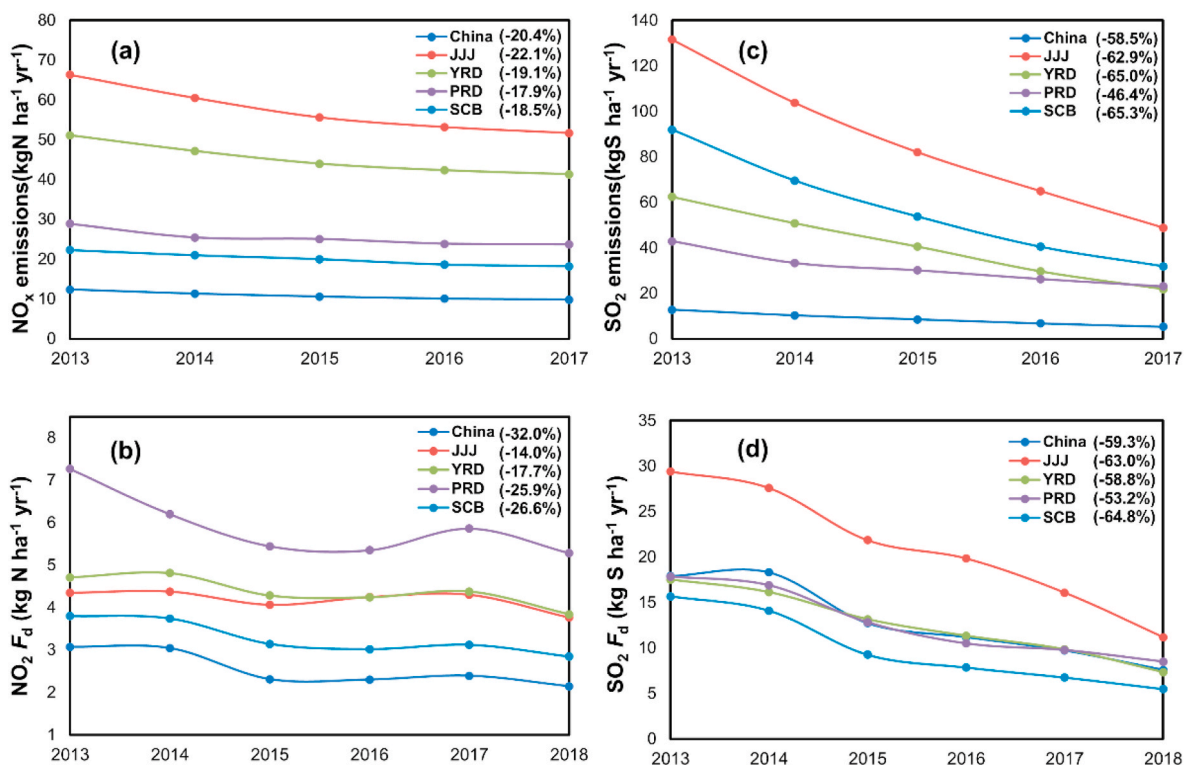


Fig. 5. The emissions and dry deposition ( $F_d$ ) of NO<sub>2</sub> (a, b) and SO<sub>2</sub> (c, d) in China and the four typical economic regions including JJJ, YRD, PRD and SCB. The numbers in the brackets are relative reductions in emissions (2013–2017) or dry deposition (2013–2018).

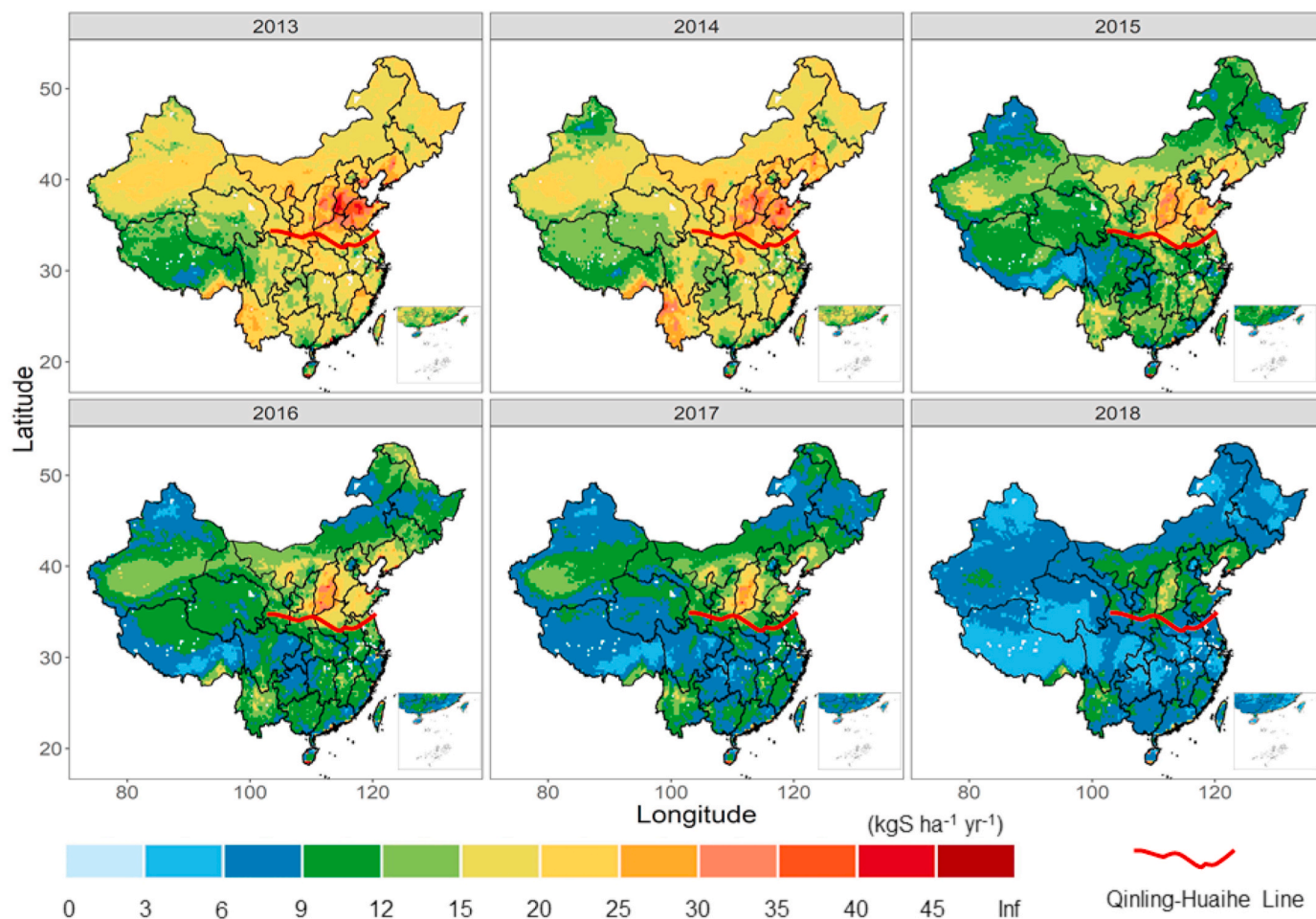


Fig. 6. The spatial distributions of SO<sub>2</sub> dry deposition flux from 2013 to 2018.

reduction rates during 2013–2018 in all the four economical developed regions were smaller than the national average at 32%. Increased transportation and industrial capacity in recent years weakened the benefit of emission controls on NO<sub>2</sub> deposition. The annual dry deposition of SO<sub>2</sub> was ranged between 7.5 and 18.4 kg S ha<sup>-1</sup> yr<sup>-1</sup>, with significantly larger value in winter than other seasons. The dry deposition in northern China was generally higher than those in the south, and it was found to decline faster during the study period as well. The relative reduction rates during 2013–2018 for two of the four economical developed regions (JJJ and SCB) were larger than the national average at 59%. The much larger reduction in SO<sub>2</sub> deposition than NO<sub>2</sub> indicated a great success of national policy on SO<sub>2</sub> control, particularly for the regions with intensive coal burning activities. To our knowledge, it is the first study that assessed the response of dry deposition of gaseous pollutants to emission reduction under NAPPACAP in China. It helps improve the understanding of the source and sink of air pollutants for scientific community, and emphasizes the importance of strengthening NO<sub>x</sub> emission control in the developed regions for policy making.

The uncertainty should be acknowledged, as the full evaluation could hardly be conducted yet on the spatiotemporal patterns of dry deposition obtained in this study. Attributed mainly to the lack of field measurements for different regions and land use types, the estimated dry deposition or  $V_d$  could not be verified with sufficient data from direct observation. Moreover, current RF model for concentration prediction relied on the data from CNEMC sites, most of which are located in urban areas. The model accuracy for rural or remote areas should be further evaluated when more observation data get available for those areas. To better quantify the deposition of typical atmospheric components across

the country, future work on data fusion with advanced statistical ensemble model is recommended to make rational use of various resources. Those contain available direct observation and CTM simulation results on the dry deposition, satellite-derived VCDs, ground-level concentrations, and geographic, meteorological and economic covariates. Moreover, it is suggested to conduct more comprehensive analysis on the source-sink relationships of typical air pollutants, including the long-term changes in the spatiotemporal patterns of emissions and deposition, and the main driving forces of the changed source-sink relationships. The outcomes can better support the policy making of limiting air pollutant emissions and reducing the ecological and environmental damages from atmospheric deposition.

#### CRediT authorship contribution statement

**Kaiyue Zhou:** Methodology, Investigation, Formal analysis, Data curation, Visualization, Software, Writing – original draft, preparation. **Yu Zhao:** Conceptualization, Methodology, Resources, Writing – review & editing. **Lin Zhang:** Software. **Mengxiao Xi:** Resources.

#### Declaration of competing interest

The authors declare that they have no known competing financial interests or personal relationships that could have appeared to influence the work reported in this paper.

## Acknowledgement

This work was sponsored by the Natural Science Foundation of China (41922052) and National Key Research and Development Program of China (2017YFC0210106). We would like to acknowledge Qiang Zhang from Tsinghua University for the emission data (MEIC), and Jintai Lin from Peking University for the satellite data (POMINO v2).

## Appendix A. Supplementary data

Supplementary data to this article can be found online at <https://doi.org/10.1016/j.atmosenv.2021.118655>.

## References

- Ban, S., Matsuda, K., Sato, K., Ohizumi, T., 2016. Long-term assessment of nitrogen deposition at remote EANET sites in Japan. *Atmos. Environ.* 146, 70–78.
- Beachley, G., Puchalski, M., Rogers, C., Lear, G., 2016. A summary of long-term trends in sulfur and nitrogen deposition in the United States: 1990–2013. *JSM Environmental Science & Ecology* 4, 1030.
- Bey, I., Jacob, D.J., Yantosca, R.M., Logan, J.A., Field, B.D., Fiore, A.M., Li, Q.B., Liu, H., Mickley, L.J., Schultz, M.G., 2001. Global modeling of tropospheric chemistry with assimilated meteorology: model description and evaluation. *Journal of Geophysical Research-Atmospheres* 106, 23073–23095.
- Breiman, L., 2001. Random forests. *Mach. Learn.* 45, 5–32.
- Chang, M., Cao, J.C., Ma, M.R., Liu, Y.M., Liu, Y.Q., Chen, W.H., Fan, Q., Liao, W.H., Jia, S.G., Wang, X.M., 2020. Dry deposition of reactive nitrogen to different ecosystems across eastern China: a comparison of three community models. *Sci. Total Environ.* 720, 137548. <https://doi.org/10.1016/j.scitotenv.2020.137548>.
- Chatzidiakou, L., Krause, A., Popoola, O.A.M., Di Antonio, A., Kellaway, M., Han, Y., Squires, F.A., Wang, T., Zhang, H., Wang, Q., Fan, Y., Chen, S., Hu, M., Quint, J.K., Barratt, B., Kelly, F.J., Zhu, T., Jones, R.L., 2019. Characterising low-cost sensors in highly portable platforms to quantify personal exposure in diverse environments. *Atmospheric Measurement Techniques* 12, 4643–4657.
- Chen, S., Zhao, Y., Zhang, R., 2018. Formation mechanism of atmospheric ammonium bisulfate: hydrogen-bond-promoted nearly barrierless reactions of SO<sub>3</sub> with NH<sub>3</sub> and H<sub>2</sub>O. *ChemPhysChem* 19, 967–972.
- China, 2018. Air Quality Targets Set by the Action Plan Have Been Fully Realized. [http://www.gov.cn/xinwen/2018-02/01/content\\_5262720.htm](http://www.gov.cn/xinwen/2018-02/01/content_5262720.htm). (Accessed 12 November 2020).
- Deng, M., Liu, L., Jiang, L., Liu, W., Wang, X., Li, S., Yang, S., Wang, B., 2018. Ecosystem scale trade-off in nitrogen acquisition pathways. *Nature Ecology & Evolution* 2, 1724–1734.
- Dentener, F., Drevet, J., Lamarque, J.F., Bey, I., Eickhout, B., Fiore, A.M., Hauglustaine, D., Horowitz, L.W., Krol, M., Kulshrestha, U.C., Lawrence, M., Galy-Lacaux, C., Rast, S., Shindell, D., Stevenson, D., Van Noije, T., Atherton, C., Bell, N., Bergman, D., Butler, T., Cofala, J., Collins, B., Doherty, R., Ellingsen, K., Galloway, J., Gauss, M., Montanaro, V., Müller, J.F., Pitari, G., Rodriguez, J., Sanderson, M., Solomon, F., Strahan, S., Schultz, M., Sudo, K., Szopa, S., Wild, O., 2006. Nitrogen and sulfur deposition on regional and global scales: a multimodel evaluation. *Global Biogeochem. Cycles* 20, 16615. <https://doi.org/10.1029/2005GB002672>.
- Ding, J.Y., Miyazaki, K., van der A, R.J., Mijling, B., Kurokawa, J.-i., Cho, S., Janssens-Maenhout, G., Zhang, Q., Liu, F., Levelt, P.F., 2017. Intercomparison of NO<sub>x</sub> emission inventories over East Asia. *Atmos. Chem. Phys.* 17, 10125–10141.
- Ebenstein, A., Fan, M.Y., Greenstone, M., He, G.J., Zhou, M.G., 2017. New evidence on the impact of sustained exposure to air pollution on life expectancy from China's Huai River Policy. *Proc. Natl. Acad. Sci. U. S. A* 114, 10384–10389.
- Engardt, M., Siniarovina, U., Khairul, N.I., Leong, C.P., 2005. Country to country transport of anthropogenic sulphur in Southeast Asia. *Atmos. Environ.* 39, 5137–5148.
- Fan, H., Zhao, C.F., Yang, Y.K., 2020. A comprehensive analysis of the spatio-temporal variation of urban air pollution in China during 2014–2018. *Atmos. Environ.* 220, 117066. <https://doi.org/10.1016/j.atmosenv.2019.117066>.
- Flechar, C.R., Nemitz, E., Smith, R.I., Fowler, D., Vermeulen, A.T., Bleeker, A., Erismann, J.W., Simpson, D., Zhang, L., Tang, Y.S., Sutton, M.A., 2011. Dry deposition of reactive nitrogen to European ecosystems: a comparison of inferential models across the NitroEurope network. *Atmos. Chem. Phys.* 11, 2703–2728.
- Geddes, J.A., Murphy, J.G., 2014. Observations of reactive nitrogen oxide fluxes by eddy covariance above two midlatitude North American mixed hardwood forests. *Atmos. Chem. Phys.* 14, 2939–2957.
- González Benítez, J.M., Cape, J.N., Heal, M.R., van Dijk, N., Díez, A.V., 2009. Atmospheric nitrogen deposition in south-east Scotland: quantification of the organic nitrogen fraction in wet, dry and bulk deposition. *Atmos. Environ.* 43, 4087–4094.
- Hicks, B.B., Baldocchi, D.D., Meyers, T.P., Hosker, R.P., Matt, D.R., 1987. A preliminary multiple resistance routine for deriving dry deposition velocities from measured quantities. *Water Air Soil Pollut.* 36, 311–330.
- Hou, X., Zhu, B., Kumar, K.R., Lu, W., 2019. Inter-annual variability in fine particulate matter pollution over China during 2013–2018: role of meteorology. *Atmos. Environ.* 214, 116842. <https://doi.org/10.1016/j.atmosenv.2019.116842>.
- Hung, H.M., Hoffmann, M.R., 2015. Oxidation of gas-phase SO<sub>2</sub> on the surfaces of acidic microdroplets: implications for sulfate and sulfate radical anion formation in the atmospheric liquid phase. *Environ. Sci. Technol.* 49, 13768–13776.
- Jia, Y.L., Yu, G.R., Gao, Y.N., He, N.P., Wang, Q.F., Jiao, C.C., Zuo, Y., 2016. Global inorganic nitrogen dry deposition inferred from ground- and space-based measurements. *Sci. Rep.* 6, 19810. <https://doi.org/10.1038/srep19810>.
- Jia, Y.L., Yu, G.R., He, N.P., Zhan, X.Y., Fang, H.J., Sheng, W.P., Zuo, Y., Zhang, D.Y., Wang, Q.F., 2014. Spatial and decadal variations in inorganic nitrogen wet deposition in China induced by human activity. *Sci. Rep.* 4, 3763. <https://doi.org/10.1038/srep03763>.
- Kang, H.Q., Zhu, B., van der A, R.J., Zhu, C.M., de Leeuw, G., Hou, X.W., Gao, J.H., 2019. Natural and anthropogenic contributions to long-term variations of SO<sub>2</sub>, NO<sub>2</sub>, CO, and AOD over East China. *Atmos. Res.* 215, 284–293.
- Ke, P., Yu, Q., Luo, Y., Kang, R., Duan, L., 2020. Fluxes of nitrogen oxides above a subtropical forest canopy in China. *Sci. Total Environ.* 715, 136993. <https://doi.org/10.1016/j.scitotenv.2020.136993>.
- Krotkov, N.A., Li, C., Leonard, P., 2015. OMI/Aura Sulfur Dioxide (SO<sub>2</sub>) Total Column L3 1 Day Best Pixel in 0.25 Degree × 0.25 Degree V3. Goddard Earth Sciences Data and Information Services Center (GES DISC), Greenbelt, MD, USA. <https://doi.org/10.5067/Aura/OMI/DATA3008>.
- Kuang, F.H., Liu, X.J., Zhu, B., Shen, J.L., Pan, Y.P., Su, M.M., Goulding, K., 2016. Wet and dry nitrogen deposition in the central Sichuan Basin of China. *Atmos. Environ.* 143, 39–50.
- Kuerban, M., Waili, Y., Fan, F., Liu, Y., Qin, W., Dore, A.J., Peng, J.J., Xu, W., Zhang, F.S., 2020. Spatio-temporal patterns of air pollution in China from 2015 to 2018 and implications for health risks. *Environ. Pollut.* 258, 113659. <https://doi.org/10.1016/j.envpol.2019.113659>.
- Li, J., 2020. Pollution trends in China from 2000 to 2017: a multi-sensor view from space. *Rem. Sens.* 12, 208. <https://doi.org/10.3390/rs12020208>.
- Lin, J.T., Martin, R.V., Boersma, K.F., Sneep, M., Stammes, P., Spurr, R., Wang, P., Van Roozendael, M., Clémer, K., Irie, H., 2014. Retrieving tropospheric nitrogen dioxide from the Ozone Monitoring Instrument: effects of aerosols, surface reflectance anisotropy, and vertical profile of nitrogen dioxide. *Atmos. Chem. Phys.* 14, 1441–1461.
- Lin, M., Oki, T., Bengtsson, M., Kanae, S., Holloway, T., Streets, D.G., 2008. Long-range transport of acidifying substances in East Asia—Part II Source–receptor relationships. *Atmos. Environ.* 42, 5956–5967.
- Liu, F., Zhang, Q., van der A, R.J., Zheng, B., Tong, D., Yan, L., Zheng, Y.X., He, K.B., 2016. Recent reduction in NO<sub>x</sub> emissions over China: synthesis of satellite observations and emission inventories. *Environ. Res. Lett.* 11, 114002. <https://doi.org/10.1088/1748-9326/11/11/114002>.
- Liu, H., Wu, B., Liu, S., Shao, P., Liu, X., Zhu, C., Wang, Y., Wu, Y., Xue, Y., Gao, J., Hao, Y., Tian, H., 2018a. A regional high-resolution emission inventory of primary air pollutants in 2012 for Beijing and the surrounding five provinces of North China. *Atmos. Environ.* 181, 20–33.
- Liu, M., Huang, X., Song, Y., Tang, J., Cao, J., Zhang, X., Zhang, Q., Wang, S., Xu, T., Kang, L., Cai, X., Zhang, H., Yang, F., Wang, H., Yu, J.Z., Lau, A.K.H., He, L., Huang, X., Duan, L., Ding, A., Xue, L., Gao, J., Liu, B., Zhu, T., 2019. Ammonia emission control in China would mitigate haze pollution and nitrogen deposition, but worsen acid rain. *Proc. Natl. Acad. Sci. U. S. A* 116, 7760–7765.
- Liu, M.X., Huang, X., Song, Y., Xu, T.T., Wang, S.X., Wu, Z.J., Hu, M., Zhang, L., Zhang, Q., Pan, Y.P., Liu, X.J., Zhu, T., 2018b. Rapid SO<sub>2</sub> emission reductions significantly increase tropospheric ammonia concentrations over the North China Plain. *Atmos. Chem. Phys.* 18, 17933–17943.
- Liu, X.J., Xu, W., Duan, L., Du, E.Z., Pan, Y.P., Lu, X.K., Zhang, L., Wu, Z.Y., Wang, X.M., Zhang, Y., Shen, J.L., Song, L., Feng, Z.Z., Liu, X.Y., Song, W., Tang, A.H., Zhang, Y. Y., Zhang, X.Y., Collett, J.L., 2017. Atmospheric nitrogen emission, deposition, and air quality impacts in China: an overview. *Current Pollution Reports* 3, 65–77.
- Liu, X.J., Xu, W., Liu, L., Du, E.Z., Shen, J.L., Luo, X.S., Zhang, X.Y., Goulding, K., 2020. Monitoring atmospheric nitrogen deposition in China. In: Liu, X.J., Du, E.Z. (Eds.), *Atmospheric Reactive Nitrogen in China*. Springer. [https://doi.org/10.1007/978-981-13-8514-8\\_3](https://doi.org/10.1007/978-981-13-8514-8_3).
- Liu, X.J., Zhang, Y., Han, W.X., Tang, A.H., Shen, J.L., Cui, Z.L., Vitousek, P., Erismann, J. W., Goulding, K., Christie, P., Fangmeier, A., Zhang, F.S., 2013. Enhanced nitrogen deposition over China. *Nature* 494, 459–462.
- Lu, X., Vitousek, P.M., Mao, Q., Gilliam, F.S., Luo, Y., Turner, B.L., Zhou, G., Mo, J., 2021. Nitrogen deposition accelerates soil carbon sequestration in tropical forests. *Proc. Natl. Acad. Sci. U. S. A* 118. <https://doi.org/10.1073/pnas.2020790118>.
- Lu, X., Zhang, L., Wu, T., Long, M.S., Wang, J., Jacob, D.J., Zhang, F., Zhang, J., Eastham, S.D., Hu, L., Zhu, L., Liu, X., Wei, M., 2020. Development of the global atmospheric chemistry general circulation model BCC-GEOS-Chem v1.0: model description and evaluation. *Geosci. Model Dev.* (GMD) 13, 3817–3838.
- Luo, X.S., Pan, Y.P., Goulding, K., Zhang, L., Liu, X.J., Zhang, F.S., 2016. Spatial and seasonal variations of atmospheric sulfur concentrations and dry deposition at 16 rural and suburban sites in China. *Atmos. Environ.* 146, 79–89.
- Lye, C., Tian, H., 2007. Spatial and temporal patterns of nitrogen deposition in China: synthesis of observational data. *Journal of Geophysical Research-Atmospheres* 112, D22S05. <https://doi.org/10.1029/2006JD007990>.
- Ma, M., Chen, W., Jia, S., Chang, M., Zhong, B., Wang, X., 2020. A new method for quantification of regional nitrogen emission - deposition transmission in China. *Atmos. Environ.* 227, 117401. <https://doi.org/10.1016/j.atmosenv.2020.117401>.
- National Bureau of Statistics of China (NBS), 2018. China Energy Statistical Yearbook. Chinese Statistics Press, Beijing (in Chinese).
- Nowlan, C.R., Martin, R.V., Phillip, S., Lamsal, L.N., Krotkov, N.A., Marais, E.A., Wang, S., Zhang, Q., 2014. Global dry deposition of nitrogen dioxide and sulfur dioxide

- inferred from space-based measurements. *Global Biogeochem. Cycles* 28, 1025–1043.
- Pan, Y.P., Wang, Y.S., Tang, G.Q., Wu, D., 2012. Wet and dry deposition of atmospheric nitrogen at ten sites in Northern China. *Atmos. Chem. Phys.* 12, 6515–6535.
- Park, R.J., 2004. Natural and transboundary pollution influences on sulfate-nitrate-ammonium aerosols in the United States: implications for policy. *J. Journal of Geophysical Research* 109. <https://agupubs.onlinelibrary.wiley.com/doi/full/10.1029/2003JD004473>.
- Shen, J., Li, Y., Liu, X., Luo, X., Tang, H., Zhang, Y., Wu, J., 2013. Atmospheric dry and wet nitrogen deposition on three contrasting land use types of an agricultural catchment in subtropical central China. *Atmos. Environ.* 67, 415–424.
- Simpson, D., Benedictow, A., Berge, H., Bergström, R., Emberson, L.D., Fagerli, H., Flechard, C.R., Hayman, G.D., Gauss, M., Jonson, J.E., Jenkin, M.E., Nyiri, A., Richter, C., Semeena, V.S., Tsyro, S., Tuovinen, J.P., Valdebenito, Á., Wind, P., 2012. The EMEP MSC-W chemical transport model – technical description. *Atmos. Chem. Phys.* 12, 7825–7865.
- Su, H., Yin, Y., Zhu, B., Wang, Z., Li, J., Pan, X., 2012. Numerical simulation and sensitive factors analyse for dry deposition of SO<sub>2</sub> and NO<sub>2</sub> in Bohai Rim area of China. *China Environ. Sci.* 32, 1921–1932 (in Chinese).
- Tan, J., Fu, J.S., Dentener, F., Sun, J., Emmons, L., Tilmes, S., Flemming, J., Takemura, T., Bian, H., Zhu, Q., Yang, C.-E., Keating, T., 2018. Source contributions to sulfur and nitrogen deposition – an HTAP II multi-model study on hemispheric transport. *Atmos. Chem. Phys.* 18, 12223–12240.
- Tao, F., Zhang, H., Hu, J., Xia, X.H., 2017. Dynamics of green productivity growth for major Chinese urban agglomerations. *Appl. Energy* 196, 170–179.
- Tarnay, L., Gertler, A.W., Blank, R.R., Taylor, G.E., 2001. Preliminary measurements of summer nitric acid and ammonia concentrations in the Lake Tahoe Basin air-shed: implications for dry deposition of atmospheric nitrogen. *Environ. Pollut.* 113, 145–153.
- Ti, C., Gao, B., Luo, Y., Wang, S., Chang, S.X., Yan, X., 2018. Dry deposition of N has a major impact on surface water quality in the Taihu Lake region in southeast China. *Atmos. Environ.* 190, 1–9.
- Tian, Y.L., Jiang, Y., Liu, Q., Xu, D.X., Zhao, S.D., He, L.H., Liu, H.J., Xu, H., 2019. Temporal and spatial trends in air quality in Beijing. *Landsc. Urban Plann.* 185, 35–43.
- Totsuka, T., Sase, H., Shimizu, H., 2005. Major activities of acid deposition monitoring network in East Asia (EANET) and related studies. In: *Plant Responses to Air Pollution and Global Change*. Springer, pp. 251–259.
- van der A, R.J., Mijling, B., Ding, J.Y., Koukouli, M.E., Liu, F., Li, Q., Mao, H.Q., Theys, N., 2017. Cleaning up the air: effectiveness of air quality policy for SO<sub>2</sub> and NO<sub>x</sub> emissions in China. *Atmos. Chem. Phys.* 17, 1775–1789.
- van Donkelaar, A., Martin, R.V., Brauer, M., Hsu, N.C., Kahn, R.A., Levy, R.C., Lyapustin, A., Sayer, A.M., Winker, D.M., 2016. Global estimates of fine particulate matter using a combined geophysical-statistical method with information from satellites, models, and monitors. *Environ. Sci. Technol.* 50, 3762–3772.
- Vet, R., Artz, R.S., Carou, S., Shaw, M., Ro, C.-U., Aas, W., Baker, A., Bowersox, V.C., Dentener, F., Galy-Lacaux, C., Hou, A., Pienaar, J.J., Gillett, R., Cristina Forti, M., Gromov, S., Hara, H., Khodzher, T., Mahowald, N.M., Nickovic, S., Rao, P.S.P., Reid, N.W., 2014. A global assessment of precipitation chemistry and deposition of sulfur, nitrogen, sea salt, base cations, organic acids, acidity and pH, and phosphorus. *Atmos. Environ.* 93, 3–100.
- Walcek, C.J., Brost, R.A., Chang, J.S., Wesely, M.L., 1986. SO<sub>2</sub>, sulfate and HNO<sub>3</sub> deposition velocities computed using regional landuse and meteorological data. *Atmos. Environ.* 20, 949–964.
- Wang, C.J., Wang, T., Wang, P.C., 2019. The spatial-temporal variation of tropospheric NO<sub>2</sub> over China during 2005 to 2018. *Atmosphere* 10, 444. <https://doi.org/10.3390/atmos10080444>.
- Wang, S., Su, H., Chen, C., Tao, W., Streets, D.G., Lu, Z., Zheng, B., Carmichael, G.R., Lelieveld, J., Poschl, U., Cheng, Y., 2020. Natural gas shortages during the “coal-to-gas” transition in China have caused a large redistribution of air pollution in winter 2017. *Proc. Natl. Acad. Sci. U. S. A.* 117, 31018–31025.
- Wei, Z., Zhang, H., Ge, H., Cai, X., Song, Y., Kang, L., 2020. Estimating the turbulent flux of the fine particulate matter by the relaxed eddy accumulation method. *Acta Sci. Circumstantiae* 40, 2400–2407 (in Chinese).
- Wesely, M.L., 1989. Parameterization of surface resistances to gaseous dry deposition in regional-scale numerical models. *Atmos. Environ.* 23 (1967), 1293–1304.
- Wu, Y., Zhang, S.J., Hao, J.M., Liu, H., Wu, X.M., Hu, J.N., Walsh, M.P., Wallington, T.J., Zhang, K.M., Stevanovic, S., 2017. On-road vehicle emissions and their control in China: a review and outlook. *Sci. Total Environ.* 574, 332–349.
- Wu, Z., Schwede, D.B., Vet, R., Walker, J.T., Shaw, M., Staebler, R., Zhang, L., 2018. Evaluation and intercomparison of five North American dry deposition algorithms at a mixed forest site. *J. Adv. Model. Earth Syst.* 10, 1571–1586.
- Xing, X., Gu, W., Liu, X., 2018. Apparel color preferences for different regions in China: the connection to personal values. *Color Res. Appl.* 43, 423–435.
- Xu, W., Liu, L., Cheng, M.M., Zhao, Y.H., Zhang, L., Pan, Y.P., Zhang, X.M., Gu, B.J., Li, Y., Zhang, X.Y., Shen, J.L., Lu, L., Luo, X.S., Zhao, Y., Feng, Z.Z., Collett Jr., J.L., Zhang, F.S., Liu, X.J., 2018a. Spatial-temporal patterns of inorganic nitrogen air concentrations and deposition in eastern China. *Atmos. Chem. Phys.* 18, 10931–10954.
- Xu, W., Luo, X.S., Pan, Y.P., Zhang, L., Tang, A.H., Shen, J.L., Zhang, Y., Li, K.H., Wu, Q. H., Yang, D.W., Zhang, Y.Y., Xue, J., Li, W.Q., Li, Q.Q., Tang, L., Lu, S.H., Liang, T., Tong, Y.A., Liu, P., Zhang, Q., Xiong, Z.Q., Shi, X.J., Wu, L.H., Shi, W.Q., Tian, K., Zhong, X.H., Shi, K., Tang, Q.Y., Zhang, L.J., Huang, J.L., He, C.E., Kuang, F.H., Zhu, B., Liu, H., Jin, X., Xin, Y.J., Shi, X.K., Du, E.Z., Dore, A.J., Tang, S., Collett Jr., J.L., Goulding, K., Sun, Y.X., Ren, J., Zhang, F.S., Liu, X.J., 2015. Quantifying atmospheric nitrogen deposition through a nationwide monitoring network across China. *Atmos. Chem. Phys.* 15, 12345–12360.
- Xu, W., Zhang, L., Liu, X.J., 2019. A database of atmospheric nitrogen concentration and deposition from the nationwide monitoring network in China. *Scientific Data* 6, 51. <https://doi.org/10.1038/s41597-019-0061-2>.
- Xu, W., Zhao, Y.H., Liu, X.J., Dore, A.J., Zhang, L., Liu, L., Cheng, M.M., 2018b. Atmospheric nitrogen deposition in the Yangtze River basin: spatial pattern and source attribution. *Environ. Pollut.* 232, 546–555.
- Xu, Y.L., Xue, W.B., Lei, Y., Zhao, Y., Cheng, S.Y., Ren, Z.H., Huang, Q., 2018c. Impact of meteorological conditions on PM<sub>2.5</sub> pollution in China during winter. *Atmosphere* 9, 429. <https://doi.org/10.3390/atmos9110429>.
- Young, M.T., Bechle, M.J., Sampson, P.D., Szpiro, A.A., Marshall, J.D., Sheppard, L., Kaufman, J.D., 2016. Satellite-Based NO<sub>2</sub> and model validation in a national prediction model based on universal Kriging and land-use regression. *Environ. Sci. Technol.* 50, 3686–3694.
- Yu, G.R., Jia, Y.L., He, N.P., Zhu, J., Chen, Z., Wang, Q.F., Piao, S.L., Liu, X.J., He, H.L., Guo, X.B., Wen, Z., Li, P., Ding, G.A., Goulding, K., 2019. Stabilization of atmospheric nitrogen deposition in China over the past decade. *Nat. Geosci.* 12, 424–431.
- Zhan, Y., Luo, Y.Z., Deng, X.F., Zhang, K.S., Zhang, M.H., Grieneisen, M.L., Di, B.F., 2018. Satellite-based estimates of daily NO<sub>2</sub> exposure in China using hybrid Random Forest and spatiotemporal Kriging model. *Environ. Sci. Technol.* 52, 4180–4189.
- Zhang, C.H., Guo, H.R., Huang, H., Ma, T.Y., Song, W., Chen, C.J., Liu, X.Y., 2021a. Atmospheric nitrogen deposition and its responses to anthropogenic emissions in a global hotspot region. *Atmos. Res.* 248, 105137. <https://doi.org/10.1016/j.atmosres.2020.105137>.
- Zhang, F., Jin, G., Li, J., Wang, C., Xu, N., 2020. Study on dynamic total factor carbon emission efficiency in China's urban agglomerations. *Sustainability* 12, 2675. <https://doi.org/10.3390/su12072675>.
- Zhang, L., Brook, J.R., Vet, R., 2003. A revised parameterization for gaseous dry deposition in air-quality models. *Atmos. Chem. Phys.* 3, 2067–2082.
- Zhang, L., Shao, J., Lu, X., Zhao, Y., Hu, Y., Henze, D.K., Liao, H., Gong, S., Zhang, Q., 2016. Sources and processes affecting fine particulate matter pollution over North China: an adjoint analysis of the Beijing APEC period. *Environ. Sci. Technol.* 50, 8731–8740.
- Zhang, Q., Zheng, Y., Tong, D., Shao, M., Wang, S., Zhang, Y., Xu, X., Wang, J., He, H., Liu, W., Ding, Y., Lei, Y., Li, J., Wang, Z., Zhang, X., Wang, Y., Cheng, J., Liu, Y., Shi, Q., Yan, L., Geng, G., Hong, C., Li, M., Liu, F., Zheng, B., Cao, J., Ding, A., Gao, J., Fu, Q., Huo, J., Liu, B., Liu, Z., Yang, F., He, K., Hao, J., 2019. Drivers of improved PM<sub>2.5</sub> air quality in China from 2013 to 2017. *Proc. Natl. Acad. Sci. U. S. A.* 116, 24463–24469.
- Zhang, S., Tison, E., Dusanter, S., Beaugard, C., Gengembre, C., Augustin, P., Fourmentin, M., Delbarre, H., Riffault, V., 2021b. Near real-time PM<sub>1</sub> chemical composition measurements at a French urban background and coastal site under industrial influence over more than a year: temporal variability and assessment of sulfur-containing emissions. *Atmos. Environ.* 244, 117960. <https://doi.org/10.1016/j.atmosenv.2020.117960>.
- Zhang, Y., Song, L., Liu, X.J., Li, W.Q., Lü, S.H., Zheng, L.X., Bai, Z.C., Cai, G.Y., Zhang, F. S., 2012. Atmospheric organic nitrogen deposition in China. *Atmos. Environ.* 46, 195–204.
- Zhang, Y., Wang, T.J., Hu, Z.Y., Xu, C.K., 2004. Temporal variety and spatial distribution of dry deposition velocities of typical air pollutants over different land-use types. *Climatic and environmental research* 9, 591–604 (in Chinese).
- Zhao, P.G., Tuygun, G.T., Li, B.L., Liu, J., Yuan, L., Luo, Y., Xiao, H., Zhou, Y.J., 2019. The effect of environmental regulations on air quality: a long-term trend analysis of SO<sub>2</sub> and NO<sub>2</sub> in the largest urban agglomeration in southwest China. *Atmospheric Pollution Research* 10, 2030–2039.
- Zhao, Y., Zhang, L., Chen, Y., Liu, X., Xu, W., Pan, Y., Duan, L., 2017. Atmospheric nitrogen deposition to China: a model analysis on nitrogen budget and critical load exceedance. *Atmos. Environ.* 153, 32–40.
- Zhao, Y., Zhang, L., Pan, Y., Wang, Y., Paulot, F., Henze, D.K., 2015. Atmospheric nitrogen deposition to the northwestern Pacific: seasonal variation and source attribution. *Atmos. Chem. Phys.* 15, 10905–10924.
- Zheng, B., Tong, D., Li, M., Liu, F., Hong, C.P., Geng, G.N., Li, H.Y., Li, X., Peng, L.Q., Qi, J., Yan, L., Zhang, Y.X., Zhao, H.Y., Zheng, Y.X., He, K.B., Zhang, Q., 2018. Trends in China's anthropogenic emissions since 2010 as the consequence of clean air actions. *Atmos. Chem. Phys.* 18, 14095–14111.
- Zhou, J., Cui, J.A., Fan, J.L., Liang, J.N., Wang, T.J., 2010. Dry deposition velocity of atmospheric nitrogen in a typical red soil agro-ecosystem in Southeastern China. *Environ. Monit. Assess.* 167, 105–113.
- Zhu, J., Chen, Z., Wang, Q., Xu, L., He, N., Jia, Y., Zhang, Q., Yu, G., 2020a. Potential transition in the effects of atmospheric nitrogen deposition in China. *Environ. Pollut.* 258, 113739. <https://doi.org/10.1016/j.envpol.2019.113739>.
- Zhu, Q., De Vries, W., Liu, X., Zeng, M., Hao, T., Du, E., Zhang, F., Shen, J., 2016. The contribution of atmospheric deposition and forest harvesting to forest soil acidification in China since 1980. *Atmos. Environ.* 146, 215–222.
- Zhu, Q., Liu, X., Hao, T., Zeng, M., Shen, J., Zhang, F., de Vries, W., 2020b. Cropland acidification increases risk of yield losses and food insecurity in China. *Environ. Pollut.* 256, 113145. <https://doi.org/10.1016/j.envpol.2019.113145>.